

PAPER

A phase-change thin film-tuned photonic crystal device

To cite this article: Longju Liu *et al* 2019 *Nanotechnology* **30** 045203

View the [article online](#) for updates and enhancements.





IOP | ebooks™

Bringing you innovative digital publishing with leading voices to create your essential collection of books in STEM research.

Start exploring the **collection** - download the first chapter of every title for free.

A phase-change thin film-tuned photonic crystal device

Longju Liu¹, Russell Mahmood², Le Wei¹, Andrew C Hillier²  and Meng Lu^{1,3} 

¹Department of Electrical and Computer Engineering, Iowa State University, Coover Hall, Ames, IA 50011, United States of America

²Department of Chemical and Biomolecular Engineering, Iowa State University, Sweeney Hall, Ames, IA 50011, United States of America

³Department of Mechanical Engineering, Iowa State University, Black Engineering, Ames, IA 50011, United States of America

E-mail: menglu@iastate.edu

Received 20 September 2018, revised 24 October 2018

Accepted for publication 1 November 2018

Published 23 November 2018



Abstract

This paper reports a tunable photonic device that incorporates a thin layer of phase-change material, $\text{Ge}_2\text{Sb}_2\text{Te}_5$ (GST), in a photonic crystal (PC) structure. The PC structure is based on a one-dimensional grating waveguide with a metal cladding. The metal-cladded PC structure supports a guided-mode resonance (GMR) that selectively absorbs light at a particular wavelength. Inserting the GST material into the gating waveguide makes it possible to control the GMR mode. Here, the GST-PC device was numerically designed and optimized to obtain significant tuning of the GMR mode around 1550 nm. The tuning phenomena were experimentally demonstrated by the heat-induced phase change between crystalline and amorphous phases of the GST thin film. A spectral shift of the resonant wavelength from 1440 to 1610 nm was achieved via the crystallization process. The phase tuning of GST exhibits good repeatability as demonstrated by switching between amorphous and crystalline phases of GST for multiple cycles. The GST-PC device represents a new approach for tuning optical resonances with potential applications including but not limited to integrated photonic circuits, optical communications, and high-performance optical filters.

Keywords: photonic crystal, tunable filter, phase-change material

(Some figures may appear in colour only in the online journal)

1. Introduction

Photonic crystal (PC) slabs that support guided-mode resonance (GMR) represent a unique class of narrowband optical filters [1–4]. A typical PC slab filter consists of a high refractive index dielectric waveguide and a one- or two-dimensional periodic grating structure. The geometry and material properties of the PC structure determine its optical characteristics, including the resonant wavelength, linewidth of the GMR, and coupling efficiency [5]. PC slab filters with narrow bandwidth and high coupling efficiency have been demonstrated for wavelengths ranging from UV to infrared [6, 7]. The resonant modes of PC devices have been exploited in many fields, such as optical communication, display, lighting, photovoltaics, and biosensing [8–18].

Recent efforts on the developments of PC slab filters have focused on technologies to achieve tuning of the GMR mode. One type of the tuning approach is to control the geometry of the PC structure. For example, the grating period or waveguide thickness of a PC device can be tuned to control the spectral signature of the GMR modes [19, 20]. Alternatively, materials with a variable refractive index can be adopted in PCs to achieve tunable GMR modes [21, 22]. For example, liquid crystals have been used as a superstrate material of a PC to module its reflectance by switching the liquid crystal's molecular alignment [23]. Tunable filters can be exploited in various applications, including optical modulation, switching, memory, and in video displays, where the transition between on or off states at a specific wavelength is required [24–28]. The

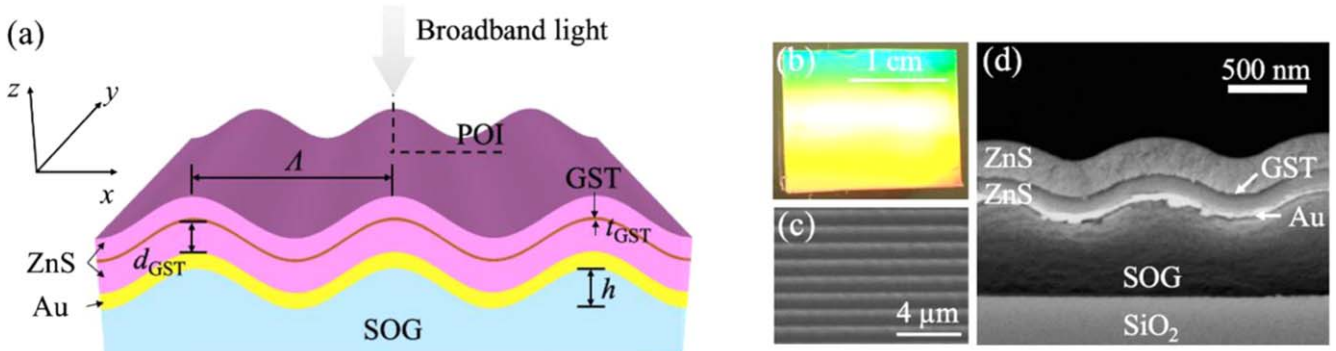


Figure 1. Grating waveguide structure with GST film. (a) Schematic diagram of the GST-PC device consisting of a sinusoidal grating and a stack of thin films. The grating is fabricated on SOG with periodicity of Λ and amplitude of h . The stack includes Au, ZnS, GST, and ZnS layers coated on top of a SOG grating. The thicknesses of GST film and its distance from the gold surface are t_{GST} and d_{GST} , respectively. (b) A photograph of the fabricated device. The overall size of the device is $18 \times 15 \text{ mm}^2$. (c) Top view SEM image and (d) cross-sectional SEM view showing the thin-film stack on the SOG grating.

performances of tunable PC filters are evaluated based on the spectral tuning range, tuning speed, and fabrication cost.

Phase-change materials (PCMs) can function as tunable electro-optical materials because of the capability of changing their electrical and optical properties between amorphous and crystalline states [29, 30]. Among the family of PCMs, $\text{Ge}_2\text{Sb}_2\text{Te}_5$ (GST) has been widely used in rewritable CD-RW discs [31]. GST also plays an important role in non-volatile phase-change memory [32, 33] and nanophotonic devices [34–38]. For photonic applications, the phase-change phenomenon of GST is particularly attractive owing to the large refractive index contrast between crystalline and amorphous phases, relatively low extinction coefficient (compared to that in the visible spectrum), rapid transition speed ($<30 \text{ ns}$), good stability at room temperature, and the ease of phase transition [35]. This paper demonstrates the application of GST as a tunable element in the PC slab filter (GST-PC).

2. Results

Figure 1(a) illustrates the structure of the tunable GST-PC. The device consists of a stack of thin films on a one-dimensional (1D) surface relief grating. The thin-film stack includes a gold cladding layer, a zinc sulfide (ZnS) waveguide layer, and a GST thin film embedded within the ZnS layer. The 1D sinusoidal grating was fabricated on a glass substrate using a spin-on-glass (SOG) and nanoimprint process [39]. In brief, a polydimethylsiloxane (PDMS) stamp was first replicated from a commercial holographic grating with a grating period of $1 \mu\text{m}$ (Edmund Optics, #40-267). To fabricate the grating using glass, a few droplets of SOG solution (Accuglass 512B, Honeywell) was spun onto a pre-oxidized Si wafer (SiO_2 thickness = 195 nm) at a spin speed of 800 rpm for 10 s . Immediately after the spin-coating, the thin SOG film was molded using the PDMS stamp under a pressure of 80 KPa . The sample, together with the PDMS stamp, was baked at 65°C on a hotplate for 3 min to solidify the SOG film. After the PDMS stamp was peeled away, the sample was then post-baked on a hotplate at 220°C overnight to solidify the SOG

with the sinusoidal grating completely. The nanoimprint process enables simple and inexpensive fabrication of sub-wavelength gratings using SOG. After patterning the SOG, the sample was deposited with a stack of Au/ZnS/GST/ZnS thin films using an e-beam evaporator (BJD-1800, Temescal) for the Au and ZnS layers and a sputter coater (ATC 1800-F, AJA International) for the GST film. Figure 1(b) is a photograph of the fabricated device over an area of $18 \times 15 \text{ mm}^2$. Scanning electron microscopy images in figures 1(c) and (d) show a top-view surface profile and cross-section of the device structure.

The ZnS film has a high refractive index ($n_{\text{ZnS}} = 2.29$ at 1550 nm) and can serve as a waveguide layer to confine light along the z -axis. The gold film ($t_{\text{Au}} = 80 \text{ nm}$) underneath the ZnS layer serves as the metal cladding boundary for the ZnS waveguide. The grating structure can couple incident light into a GMR mode supported by the ZnS grating waveguide. At the resonant wavelength (λ_r), light is strongly absorbed owing to optical losses in the gold cladding. In contrast, the gold layer effectively reflects light at other wavelengths that do not meet the resonant condition. Therefore, the metal-cladding PC supports a narrowband resonant absorption, which manifests as a reflection minimum at the resonance condition [40].

To tune the GMR mode, a thin film of GST is integrated into the ZnS grating waveguide. The thickness of GST and its position on the ZnS waveguide are optimized to maximize the effect of the phase transition on the resonant signatures. By inducing phase transitions between crystalline and amorphous states of GST, the effective refractive index for the waveguide can be modulated, and thus, shift GMR modes in the reflection spectrum.

2.1. Tuning of optical resonances of the metal-cladding GMR device

Rigorous coupled wave analysis (RCWA, DiffractMOD, Synopsys Inc.) was used to facilitate the device design. Optical characteristics, including reflection spectra and field distributions, were calculated using measured optical

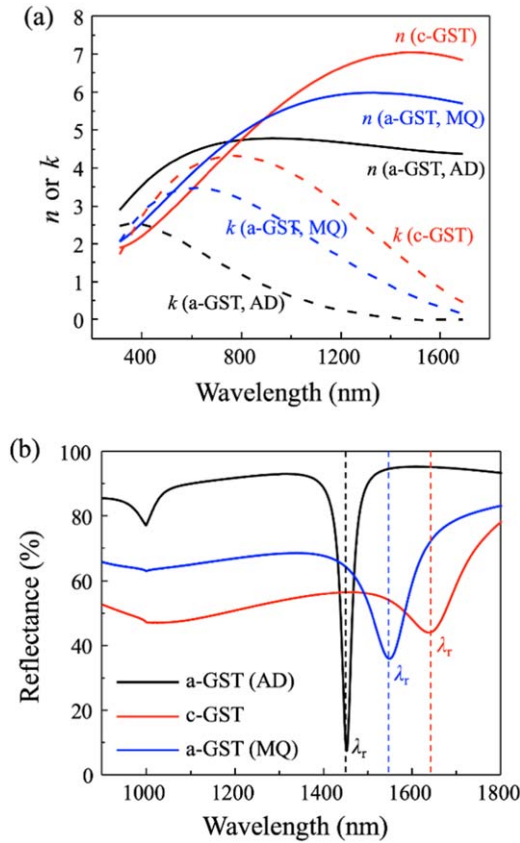


Figure 2. Measured n , k for GST and calculated reflection spectra for GST-PC. (a) Measured refractive indices (n , solid lines) and extinction coefficients (k , dashed lines) in the near infrared wavelength range: n (solid lines) and k (dash lines) for the as-deposited (AD) amorphous GST (black), crystalline GST (c-GST, red), and melt-quenched (MQ) amorphous GST (a-GST, blue). A detailed description of the spectroscopic ellipsometry measurement can be found in the supporting information. (b) Simulation results of the reflection spectra for GST-PC devices integrated with GST thin film in as-deposited amorphous (black), crystalline (red) states and melt-quenched amorphous GST (blue).

constants and device dimensions with the GST film in the amorphous and crystalline states. The device is designed to operate in the near IR telecom window, where GST has relatively small material loss and exhibits a large change in refractive index during phase transition. In the RCWA simulation, the refractive index and extinction coefficient of the GST were from the results of ellipsometry measurement and fitted by the multi-coefficient Lorentz–Drude model as shown in figure 2(a). The optical properties of Au, ZnS, and glass layers were taken from Johnson and Christy’s handbook [41]. The simulation domain was set to one period of the grating with periodic boundary condition imposed on the x -axis. The glass substrate was truncated and treated as a semi-infinite plane. The device was illuminated with a normally incident, unit magnitude plane wave propagating in the z -axis. The incident light was polarized along the y -axis (figure 1(a)), which can excite transverse-electric (TE) GMR modes. To obtain GMR modes around 1550 nm, the period and depth of

the sinusoidal grating were chosen as $\Lambda = 1 \mu\text{m}$ and $h = 150 \text{ nm}$, respectively.

To investigate the impact of the phase transition in the GST film on the GMR mode, device designs with several different GST thicknesses (t_{GST}) and positions (d_{GST}) in the ZnS waveguide were modeled. We first set $t_{\text{GST}} = 8.5 \text{ nm}$ and the ZnS thickness to $t_{\text{ZnS}} = 200 \text{ nm}$. The position of the d_{GST} denotes the distance of GST film from the gold cladding. The GST film is located in between the gold cladding and the ZnS waveguide when $d_{\text{GST}} = 0$ and on top of the ZnS waveguide when $d_{\text{GST}} = 200 \text{ nm}$. At intermediate values of d_{GST} the GST film is embedded within the thicker ZnS layer. The value of d_{GST} was increased from 0 to 200 nm. For $d_{\text{GST}} = 135 \text{ nm}$, the calculated reflection spectra for as-deposited a-GST, c-GST and melt-quenched a-GST are shown in figure 2(b). The dips in the reflection spectra represent the absorption resonance conditions for the metal-cladded GMR mode. The shift of the resonant wavelength ($\Delta\lambda_r$) is defined as the change in the wavelength of the reflection minimum when the GST film transforms from the amorphous to crystalline state.

Calculated values of $\Delta\lambda_r$ are plotted for the GST-PC device as a function of d_{GST} in figure 3(a). It can be seen that the resonant wavelength shift approaches zero when $d_{\text{GST}} = 0$ (red circle). The phenomenon can be explained by considering that the tangential electric field vanishes at metal surface and, thus, the GMR mode is insensitive to the phase transition. Moving the GST film away from the metal cladding increases the resonance wavelength shift until the shift reaches its maximum near $d_{\text{GST}} = 175 \text{ nm}$. After the maximum point, $\Delta\lambda_r$ decreases slightly until the GST layer is located on top of the ZnS layer at $d_{\text{GST}} = 200 \text{ nm}$. It can be seen that the phase transition results in a resonant wavelength shift over 200 nm when $125 \text{ nm} < d_{\text{GST}} < 200 \text{ nm}$ (the blue region). Meanwhile, within the blue region, the change of λ_r as a function of d_{GST} is small. The electric field distributions $|E_y(x, z)|^2$ near the grating surface with of GST films at three different GST locations ($d_{\text{GST}} = 0, 135$, and 200 nm) are plotted in figure 3(b). The resonance conditions with a-GST are shown at $\lambda_r = 1360, 1440$ and 1460 nm , respectively. From figure 3(b), we can see that the near-field distributions of the GMR mode do not alter dramatically for these three cases. The change of near-field profile with regard to the GST position is negligible. According to figures 3(a) and (b), the resonant wavelength shift upon phase transition is larger when the GST layer is placed at the position, where the electric field is stronger. In the GST-PC design, the GST film is embedded within the ZnS waveguide with $d_{\text{GST}} \sim 135 \text{ nm}$ to maximize the tuning effect. Meanwhile, the top layer of ZnS can also serve as a protection and passivation layer for the GST film.

The thickness of the GST layer also plays an important role in the tuning capability. As illustrated in figure 2(a), both the real and imaginary parts of the refractive index exhibit significant changes when the GST film switches between the amorphous and crystalline states. Although it is possible to

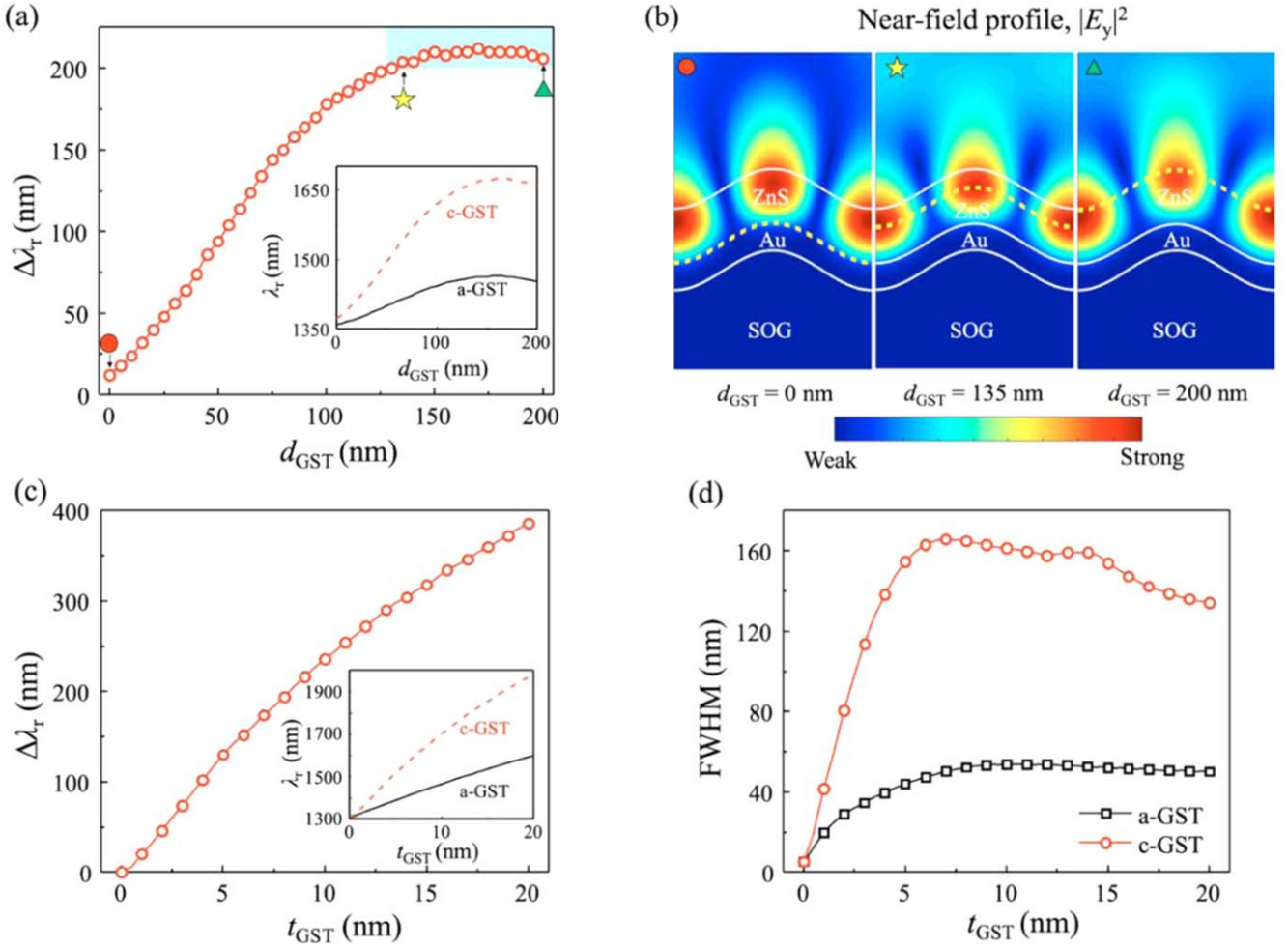


Figure 3. Phase change-induced shift of resonance wavelength. (a) Calculated $\Delta\lambda_r$ versus the position of the GST thin film within the 200 nm thick ZnS waveguide. Inset: the resonant wavelength for GST-PC with amorphous (black solid line) and crystalline GST thin films (red dash line) as a function of d_{GST} . (b) Electric field profiles for GST-GMR device with GST film located at three different positions ($d_{GST} = 0$ nm, $d_{GST} = 135$ nm and $d_{GST} = 200$ nm). The yellow dash curves denote the location of GST thin film. (c) Calculated $\Delta\lambda_r$ as a function of GST thickness. Inset: the resonant wavelength for GST-PC with amorphous (black solid line) and crystalline GST thin films (red dash line) as a function of t_{GST} . (d) Calculated FWHMs for the GMR modes for the designs with a-GST (black square) and c-GST (red circle), respectively.

obtain a measurable shift in the GMR mode with just a few nanometer-thick GST film, a thicker film produces a much larger spectral shift. On the other hand, since the GST film exhibits strong optical loss at the target wavelength range, an excessively thick GST film may quench the optical resonance. To investigate the trade-off, we calculated the device resonances with the t_{GST} ranging from 0 to 20 nm. The resonant wavelength as function of t_{GST} for a-GST and c-GST are plotted in the inset of figure 3(c). These results show that the difference between the a-GST and c-GST resonances increases when the GST film thickness increases. Figures 3(d) and (d) summarize the shift of resonant wavelengths and the full width half maximum (FWHM) of the reflection minima. The FWHM values reach their maximum values at $t_{GST} = 10$ nm for a-GST and $t_{GST} = 7$ nm for c-GST, respectively. When $t_{GST} > 10$ nm, both FWHM curves decrease slightly. This can be explained by the decrease of the GST extinction coefficient (k_{GST}) from 900 to 1700 nm. As the GST thickness increases, the GMR mode shifts to longer wavelengths, where

the k_{GST} values continue decreasing for both a-GST and c-GST, as shown in figure 2(a). The loss caused by material absorption is therefore mitigated, resulting the decrease of FWHM. The modeling results indicate that as long as the GST thickness is larger than $t_{GST} = 7.5$ nm, a wavelength shift that is greater than the FWHM of either a-GST or c-GST phase can be obtained. A GST thickness of $t_{GST} = 8.5$ nm was selected for our device to achieve the tuning in the desired wavelength range (~ 1400 to ~ 1600 nm) with a relatively small FWHM and large wavelength shift.

2.2. Tuning of GMR mode by the phase transition of GST

Based on the RCWA modeling results, we fabricated the GST-PC device with $\Lambda = 1000$ nm and $d_{GST} = 135$ nm as shown in figures 1(b)–(d). The thicknesses of gold film, ZnS, GST, and ZnS films are $t_{Au} = 80$ nm, and $t_{ZnS1} = 135$ nm, $t_{GST} = 8.5$ nm, and $t_{ZnS2} = 65$ nm, respectively. A test system was built to control the phase transition of the GST film

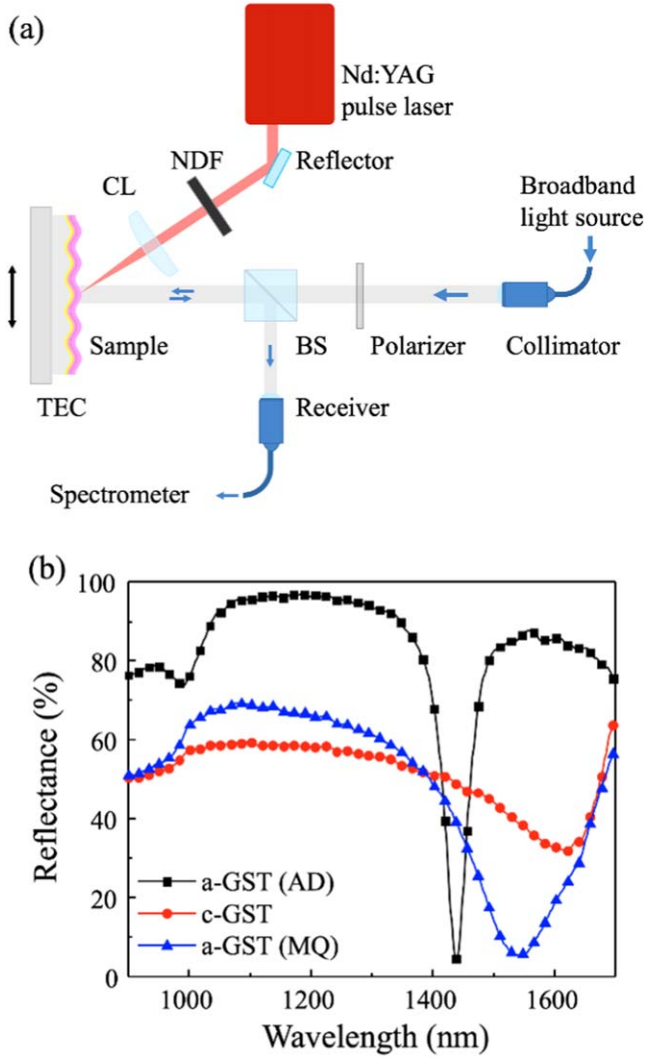


Figure 4. (a) Schematic of the optical setup for reflection measurement and laser line-scanning apparatus. The sample is mounted on a thermoelectric cooler (TEC), which can control the sample temperature. The laser line-scanning setup consists of a pulse Nd:YAG laser, a dielectric mirror, a neutral density filter (NDF), and a cylindrical lens. The linearly polarized broadband light is used as the excitation to measure the sample reflection. The reflected light is directed to a near infrared spectrometer using a beam splitter (BS). (b) Measured reflection spectra for the GST-PC with as-deposited a-GST (black), c-GST (red), and melt-quenched GST (blue) layers, respectively.

and characterize the sample response. As shown in figure 4(a), the device is illuminated by a collimated, TE-polarized broadband light source (HL-2000, OceanOptics) from a fiber at normal incidence. It is worth noting that the resonant features are also dependent on the angle of incidence. To focus on the study of GST-induced tuning, we kept the excitation at normal incidence. The excitation beam was incident onto the GST-PC device via a non-polarizing 50/50 beam splitter cube. The reflected light is collected through the beam splitter with a second fiber and analyzed using a NIR spectrometer (StellarNet Inc.). The spectral range of the spectrometer is 897–1788 nm. The reflectance was calculated against a gold-coated mirror as the reference spectrum. To

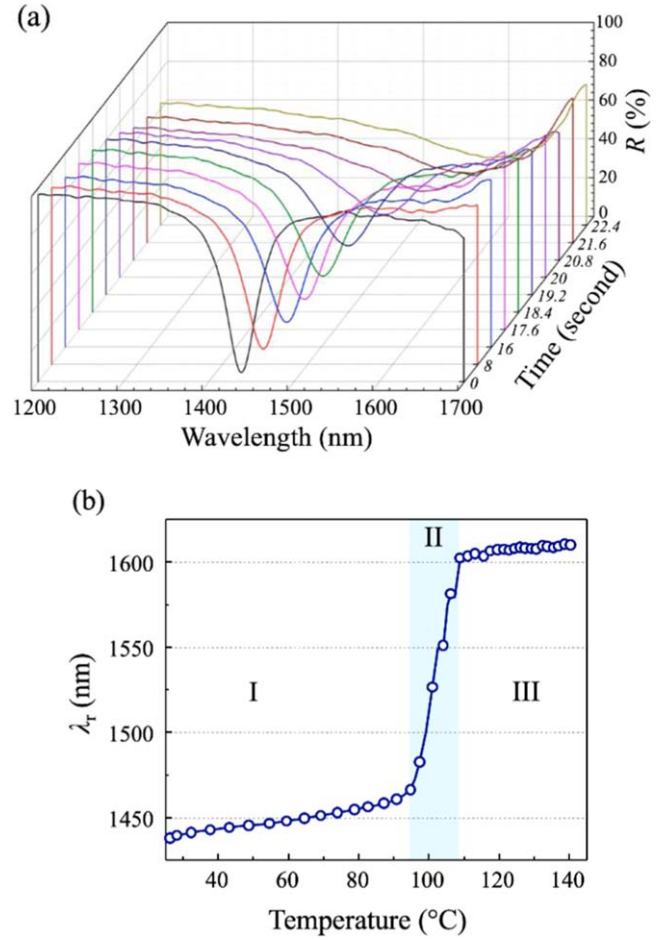


Figure 5. Measured GMR mode versus temperature. (a) Waterfall plot of ten selected reflection spectra of GST-PC in the progress when the as-deposited amorphous GST layer was being transitioned into crystalline phase using TEC heating. The spectra were recorded every 200 ms for a period of 22.4 s. The broadening of the reflection dip was observed. (b) Shift of resonant wavelength as a function of temperature. The resonant wavelength increases dramatically during the phase transition of GST (highlighted by the region shaded in blue).

identify the resonant wavelength, we used a second polynomial function to fit 20 data points near the minimal transmittance point.

2.2.1. Heat-induced crystallization. The reflection spectrum of the device with the sputtered amorphous GST was measured and is shown in figure 4(b). To induce its crystallization, the GST film must be heated above its crystallization temperature (T_c) but cannot exceed the melting temperature (T_m) [25, 26]. We used a thermoelectric cooler (TEC, Marlow TG12-4L) to heat the GST-PC by mounting it on the hot side of the TEC. We measured the reflection spectra every 200 ms during the heating cycle. Measured reflection spectra at several time steps are shown in figure 5(a). A continuous shift of the GMR mode from 1440 to 1610.5 nm is observed in a time span of 22.4 s. The phase transition from a-GST to c-GST also broadens the FWHM of the GMR mode from 49.0 to 187.9 nm. The results indicate that both n_{GST} and k_{GST} increase with the temperature,

as expected based upon the underlying crystallization process of GST.

The temperature of the device was recorded during heating using a thermocouple. The measured resonant wavelength vs. temperature curve is plotted in figure 5(b). There are three distinct regions observed during the temperature rise. In Region I, where the temperature was below $\sim 93^\circ\text{C}$, the resonance wavelength shifts slowly from 1439 to 1461 nm at a rate of $0.2\text{ nm }^\circ\text{C}^{-1}$ after the TEC was turned on. Above 93°C (Region II), λ_r shifts rapidly from 1461 to 1603 nm at a rate approaching $9.3\text{ nm }^\circ\text{C}^{-1}$, indicating a quick phase transition from amorphous to crystalline state. The resonant wavelength gradually stabilizes (Region III), near 1610.5 nm, suggesting that the GST layer has been fully crystallized.

2.2.2. Pulse laser-induced amorphization. To switch the GST film from its crystalline state back to the amorphous state, it is necessary to heat the GST above its melting temperature and cool it down fast enough to achieve the melt-quenched a-GST film [29, 30]. As demonstrated in previous works [38, 42], ultrafast pulse lasers are well suited for such a task. In this work, we utilized a Q-switched Nd:YAG laser (Oppolette 3043, OPOTEK Inc.) to initiate the crystalline to amorphous transition for the c-GST film. The laser outputs 7 ns pulses at 1064 nm with a beam diameter of 3 mm. Due to speckling in the laser beam, direct exposure of the device led to a spatially non-uniform transition. To minimize this non-uniformity, we focused the laser beam into a 3 mm long and $20\text{ }\mu\text{m}$ wide line using a cylindrical lens (focal length = 35 mm). The laser fluence and repetition rate were set at $285\text{ }\mu\text{J cm}^{-2}$ and 20 Hz, respectively. The device was mounted on a motorized translation stage and scanned through the laser line in order to expose the desired area. The scanning speed was adjusted to match the repetition rate of the pulse laser. Each scan generated an area of $3\text{ mm} \times 3\text{ mm}$ on the device. The reflection spectrum was then measured after the scanning process. Figure 4(b) compares the reflectance of the device with the as-deposited a-GST, c-GST, and the melt-quenched a-GST films. The reflection dip of melt-quenched a-GST is not able to shift back to the initial position of the as-deposited a-GST. This phenomenon is expected since figure 2(b) shows that the complex refractive index of melt-quenched a-GST is different from that of the as-deposited a-GST. Previous work reported by other researchers also showed that the melt-quenched a-GST has different electrical and optical properties compared to the as-deposited a-GST [43].

To study the reparability of GST tuning, we tested the dynamics and repeatability of the crystallization and melt-quench transition processes, which were repeated for multiple cycles. For each cycle, the device was heated using the TEC and subsequently scanned using the pulsed laser. Reflection spectra were recorded every 200 ms during the crystallization process and then paused during the melt quenching. The resonant wavelengths were determined as a function of time. Results of the first six cycles are summarized in figure 6. The

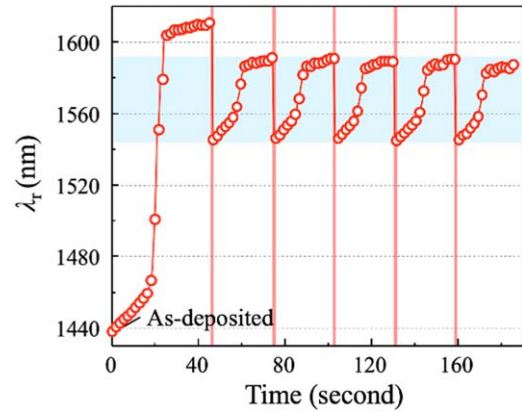


Figure 6. Tuning of GMR mode during six cycles of phase transitions. The transitions from c-GST to a-GST are labeled by the vertical red line, where the sample was scanned by the pulse laser. The substrate temperature was set at room temperature during the re-amorphizations. The sample was heated above GST's crystallization temperature during each cycle and the reflection spectra were measured every 200 ms.

cycling experiment started with the device consisting of the as-deposited a-GST film with the initial resonant wavelength located at 1440 nm. The first crystallization process shifted the resonant wavelength to 1610 nm and the subsequent melt-quenched process moved the resonance back to 1544 nm. During the following cycles, the resonance wavelength was modulated in the range of 1544–1592 nm, as highlighted in the shadow area in figure 6.

3. Conclusions

In summary, we have designed and fabricated a GST-PC device that exhibits tunable resonant modes in the $1.55\text{ }\mu\text{m}$ band of telecom wavelength. The GST-PC device consists of a metal-cladding leaky mode waveguide and incorporated a thin layer of GST. Tuning of the resonance wavelength between 1440 and 1610 nm was achieved by switching the GST between its crystalline and amorphous states. The refractive index and extinction values of the sputtered amorphous GST, crystallized GST, and quenched melt GST films were characterized using ellipsometry in the near infrared wavelength range. The RCWA simulation was used to numerically design and optimize the GST-PC tunable filter. To investigate the phase change-induced tuning phenomena, we implemented a line-scanning platform with which we successfully induced crystallization for amorphous GST by TEC heating and re-amorphization to crystallized GST using a Q-switch pulsed laser. The reliability and repeatability of our device was also demonstrated by cycling the GST film between its crystalline and amorphous states.

Although the tuning of PC resonance has been successful, the resonance linewidth significantly increased when the GST film was set at its crystalline phase. The broadening of the resonance linewidth is likely due to the high material loss of the c-GST film. To minimize the broadening effect, it is

important to select a PCM film with low material loss in both crystalline and amorphous states. For example, we could replace the GST film using the $\text{Ge}_2\text{Sb}_2\text{Se}_4\text{Te}_1$ film recently demonstrated by Zhang *et al* to maintain narrowband features during a tuning process [44]. This work focuses on the optical tuning of GST film using the pulsed laser, and our future work will test the control of the GST film using electrical pulses.

Acknowledgments

This work was supported by the National Science Foundation under Award No. ECCS 16-53673. Any opinions, findings, and conclusions or recommendations expressed in this material are those of the author(s) and do not necessarily reflect the views of the National Science Foundation. LL acknowledges the Catron Foundation Graduate Fellowship for financial support. We would like to thank Dr Liang Dong for providing the pulse laser. The authors declare no competing financial interests.

ORCID iDs

Andrew C Hillier  <https://orcid.org/0000-0002-2729-1368>

Meng Lu  <https://orcid.org/0000-0001-7444-6759>

References

- [1] Wang S S, Moharam M G, Magnusson R and Bagby J S 1990 Guided-mode resonances in planar dielectric-layer diffraction gratings *J. Opt. Soc. Am. A* **7** 1470
- [2] Day R W, Wang S S and Magnusson R 1996 Filter-response line shapes of resonant waveguide gratings *J. Lightwave Technol.* **14** 1815–24
- [3] Neviere M, Petit R and Cadilhac M 1973 About the theory of optical grating coupler-waveguide systems *Opt. Commun.* **8** 113–7
- [4] Popov E, Mashev L and Maystre D 1986 Theoretical study of the anomalies of coated dielectric gratings *Opt. Acta* **33** 607–19
- [5] Liu J-N, Schulmerich M V, Bhargava R and Cunningham B T 2011 Optimally designed narrowband guided-mode resonance reflectance filters for mid-infrared spectroscopy *Opt. Express* **19** 24182
- [6] Liu J-N, Schulmerich M V, Bhargava R and Cunningham B T 2014 Sculpting narrowband Fano resonances inherent in the large-area mid-infrared photonic crystal microresonators for spectroscopic imaging *Opt. Express* **22** 18142
- [7] Ganesh N and Cunningham B T 2006 Photonic-crystal near-ultraviolet reflectance filters fabricated by nanoreplica molding *Appl. Phys. Lett.* **88** 7–9
- [8] Magnusson R and Shokoh-Saremi M 2007 Widely tunable guided-mode resonance nanoelectromechanical RGB pixels *Opt. Express* **15** 10903–10
- [9] Uddin M J, Khaleque T and Magnusson R 2014 Guided-mode resonant polarization-controlled tunable color filters *Opt. Express* **22** 12307
- [10] Cunningham B, Li P, Lin B and Pepper J 2002 Colorimetric resonant reflection as a direct biochemical assay technique *Sensors Actuators B* **81** 316–28
- [11] Wawro D, Tibuleac S, Magnusson R and Liu H 2000 Optical fiber endface biosensor based on resonances in dielectric waveguide gratings *Proc. SPIE* **3911** 86–94
- [12] Luo S, Chen L, Bao Y, Yang N and Zhu Y 2013 Non-polarizing guided-mode resonance grating filter for telecommunications *Optik* **124** 5158–60
- [13] Mehta A A, Rumpf R C, Roth Z A and Johnson E G 2007 Guided mode resonance filter as a spectrally selective feedback element in a double-cladding optical fiber laser *IEEE Photonics Technol. Lett.* **19** 2030–2
- [14] Polman A and Atwater H A 2012 Photonic design principles for ultrahigh-efficiency photovoltaics *Nat. Mater.* **11** 174–7
- [15] Chaudhery V, George S, Lu M, Pokhriyal A and Cunningham B T 2013 Nanostructured surfaces and detection instrumentation for photonic crystal enhanced fluorescence *Sensors* **13** 5561–84
- [16] Chen W, Long K D, Lu M, Chaudhery V, Yu H, Choi J S, Polans J, Zhuo Y, Harley B A C and Cunningham B T 2013 Photonic crystal enhanced microscopy for imaging of live cell adhesion *Analyst* **138** 5886–94
- [17] Pokhriyal A, Lu M, Chaudhery V, Huang C-S, Schulz S and Cunningham B T 2010 Photonic crystal enhanced fluorescence using a quartz substrate to reduce limits of detection *Opt. Express* **18** 24793–808
- [18] Niraula M, Yoon J W and Magnusson R 2015 Single-layer optical bandpass filter technology *Opt. Lett.* **40** 5062–5
- [19] Liu L, Khan H A, Li J, Hillier A C and Lu M 2016 A strain-tunable nanoimprint lithography for linear variable photonic crystal filters *Nanotechnology* **27** 295301
- [20] Dobbs D W, Gershkovich I and Cunningham B T 2006 Fabrication of a graded-wavelength guided-mode resonance filter photonic crystal *Appl. Phys. Lett.* **89** 123113
- [21] Qian L, Zhang D, Dai B, Huang Y, Tao C, Hong R and Zhuang S 2015 Electrically driving bandwidth tunable guided-mode resonance filter based on a twisted nematic liquid crystal polarization rotator *Opt. Lett.* **40** 713–6
- [22] Wang Q, Zhang D, Huang Y, Ni Z, Chen J, Zhong Y and Zhuang S 2010 Type of tunable guided-mode resonance filter based on electro-optic characteristic of polymer-dispersed liquid crystal *Opt. Lett.* **35** 1236–8
- [23] Lu C and Lipson R H 2010 Interference lithography: a powerful tool for fabricating periodic structures *Laser Photonics Rev.* **4** 568–80
- [24] Xiao S, Wang T, Liu T, Yan X, Li Z and Xu C 2018 Active modulation of electromagnetically induced transparency analogue in terahertz hybrid metal-graphene metamaterials *Carbon* **126** 271–8
- [25] Liu T, Wang H, Liu Y, Xiao L, Zhou C, Liu Y, Xu C and Xiao S 2018 Independently tunable dual-spectral electromagnetically induced transparency in a terahertz metal-graphene metamaterial *J. Phys. D: Appl. Phys.* **51** 415105
- [26] Xiao S, Wang T, Jiang X, Yan X, Cheng L, Wang B and Xu C 2017 Strong interaction between graphene layer and Fano resonance in terahertz metamaterials *J. Phys. D: Appl. Phys.* **50** 195101
- [27] Jiang X, Wang T, Xiao S, Yan X, Cheng L and Zhong Q 2018 Approaching perfect absorption of monolayer molybdenum disulfide at visible wavelengths using critical coupling *Nanotechnology* **29** 335205
- [28] Rude M, Pello J, Simpson R E, Osmond J, Roelkens G, van der Tol J J G M and Pruneri V 2013 Optical switching at 1.55 μm in silicon racetrack resonators using phase change materials *Appl. Phys. Lett.* **103** 141114–9
- [29] Raoux S 2009 Phase change materials *Annu. Rev. Mater. Res.* **39** 25–48

- [30] Wuttig M and Yamada N 2007 Phase change materials for rewriteable data storage *Nat. Mater.* **6** 824–32
- [31] Ohta T 2001 Phase-change optical memory promotes the DVD optical disk *J. Optoelectron. Adv. Mater.* **3** 609–26
- [32] Raoux S, Xiong F, Wuttig M and Pop E 2014 Phase change materials and phase change memory *MRS Bull.* **39** 703–10
- [33] Burr G W *et al* 2010 Phase change memory technology *J. Vac. Sci. Technol. B* **28** 223–62
- [34] Appavoo K and Haglund R F 2014 Polarization selective phase-change nanomodulator *Sci. Rep.* **4** 1–6
- [35] Wetnic W and Wuttig M 2008 Reversible switching in phase-change materials *Mater. Today* **11** 20–7
- [36] Yoo S, Gwon T, Eom T, Kim S and Hwang C S 2016 Multicolor changeable optical coating by adopting multiple layers of ultrathin phase change material film *ACS Photonics* **3** 1265–70
- [37] Chen Y, Li X, Luo X, Maier S A and Hong M 2015 Tunable near-infrared plasmonic perfect absorber based on phase-change materials *Photonics Res.* **3** 54
- [38] Rudé M, Mkhitarian V, Cetin A E, Miller T A, Carrilero A, Wall S, de Abajo F J G, Altug H and Pruneri V 2016 Ultrafast and broadband tuning of resonant optical nanostructures using phase-change materials *Adv. Opt. Mater.* **4** 1060–6
- [39] Huang Y, Liu L, Johnson M, C Hillier A and Lu M 2016 One-step sol-gel imprint lithography for guided-mode resonance structures *Nanotechnology* **27** 095302
- [40] Zourob M and Goddard N J 2005 Metal clad leaky waveguides for chemical and biosensing applications *Biosens. Bioelectron.* **20** 1718–27
- [41] Johnson P B and Christy R W 1972 Optical constants of the noble metals *Phys. Rev. B* **6** 4370–9
- [42] Appavoo K, Wang B, Brady N F, Seo M, Nag J, Prasankumar R P, Hilton D J, Pantelides S T and Haglund R F 2014 Ultrafast phase transition via catastrophic phonon collapse driven by plasmonic hot-electron injection *Nano Lett.* **14** 1127–33
- [43] Waldecker L, Miller T A, Rudé M, Bertoni R, Osmond J, Pruneri V, Simpson R E, Ernstorfer R and Wall S 2015 Time-domain separation of optical properties from structural transitions in resonantly bonded materials *Nat. Mater.* **14** 991–5
- [44] Zhang Y *et al* 2017 Broadband transparent optical phase change materials *2017 Conf. on Lasers and Electro-Optics (CLEO)* (https://doi.org/10.1364/CLEO_AT.2017.JTh5C.4)